Energy & Environmental Science

Accepted Manuscript

This article can be cited before page numbers have been issued, to do this please use: H. Xu, R. Zhang, D. Luo, K. Huang, J. Wang, G. Sun, H. Dou and X. Zhang, *Energy Environ. Sci.*, 2025, DOI: 10.1039/D5EE02593A.

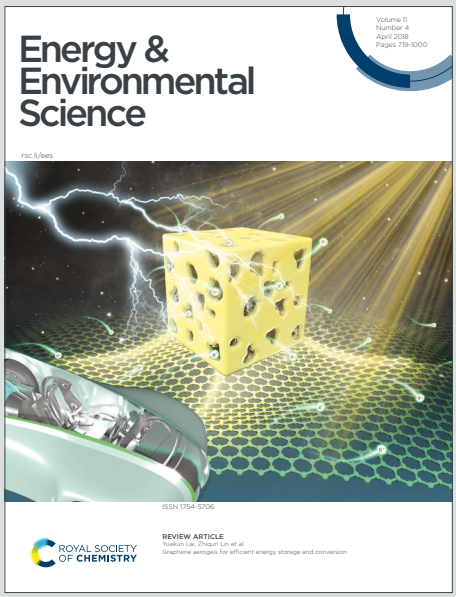

ROYAL SOCIETY OF CHEMISTRY

rsc.li/ees

View Article Online
DOI: 10.1039/D5EE02593A

Broader context statement

Recently, Zn-iodine batteries composed of Zn metal anode and iodine/host cathode receive worldwide attentions because of their Earth-abundance, high theoretical capacities and stable potential plateau. However, the shuttle effect of polyiodides and aggregation of solid iodine on the cathode surface in aqueous Zn-iodine batteries are considered as the main issues for unsatisfactory cycling stability and slow charge transfer kinetics, respectively. Though many efforts are devoted to solving the above issues, the state-of-the-art strategies remain great challenge to simultaneously inhibit polyiodides shuttle and reform the deposition of solid iodine. Herein, we develop a biphasic electrolyte composed of immiscible organic and aqueous solvents for stable Zn-iodine batteries. Specifically, the co-extraction of iodine and polyiodides is experimentally achieved and the mechanism is correlated to the principle of polarity coupling, effectively restricting I-species in organic phase. Moreover, the electrochemical redox reactions of iodine/polyiodides at cathodic side (organic phase) follow liquid-liquid conversion route is explored, which are distinct from the formation of solid iodine passivation layer in aqueous electrolyte and significantly enhance charge transfer kinetics.

Polarity Coupling in Biphasic Electrolyte Enables Iodine/Polyiodides Co-Extraction for Portable Zn-Iodine Batteries Following Liquid-Liquid Conversion Route

Received 00th January 20xx,
Accepted 00th January 20xx

DOI: 10.1039/x0xx00000x

Hai Xu[a,b], Ruanye Zhang[a], Derong Luo[a], Kangsheng Huang[a], Jiuqing Wang[a], Gengzhi Sun[b]*, Hui Dou[a,c]*, Xiaogang Zhang[a,c]*

The shuttle effect of polyiodides and aggregation of solid iodine on the cathode surface in aqueous Zn-iodine batteries are considered as the main issues for unsatisfactory cycling stability and slow charge transfer kinetics, respectively. Herein, we develop a biphasic (BP) electrolyte composed of immiscible organic (ethyl acetate, EA) and aqueous solvents for the co-extraction of iodine/polyiodides. The underlying mechanism is clarified by the principle of polarity coupling between iodine species and solvent molecules. Notably, distinct from the formation of solid iodine in aqueous electrolyte, the electrochemical redox reactions of iodine/polyiodides at the cathodic side (organic phase) investigated by rotating ring electrode follow the liquid-liquid conversion route. Accordingly, the diffusion of polyiodides is effectively suppressed at the interface of BP electrolyte and the absence of solid iodine deposition significantly enhances charge transfer kinetics. Moreover, the quasi-solid-state Zn-iodine batteries featuring with gravity-independent stratified architecture is demonstrated, enabled by a BP systems consisting of microspace-confined EA and PAM-CMC hydrogel. The fabricated portable devices exhibit an areal capacity of 1.40 mAh cm^{-2} at 1 mA cm^{-2}, improved rate performance and stable cycling performance over 22,000 cycles at 10 mA cm^{-2}, indicating extraordinary reliability for wearable applications.

Introduction

The rapid development of portable/wearable electronics, driven by growing demands of wireless communication, smart human-machine-interfaces, artificial intelligence, humanoid robotics and unmanned aerial vehicles, has led to the exploitation of advanced energy storage devices with the expected features of high effectiveness, low-cost and long serving lifespan[1-4]. Although lithium ion batteries (LIBs) have been commercialized for over 30 years and are considered the primary choice as power supplier in existing consumable electronics and electric vehicles, the critical challenge in terms of scarce resources of Li-salt undoubtedly hinders their sustainable availability[5-8]. In this instance, great efforts are required to devote to pursuing alternative substitutions. Among all potential candidates, Zn-iodine batteries composed of Zn metal anode and iodine/host cathode receive worldwide attention because of their Earth-abundance, high theoretical capacities and stable potential plateau[9-12].

In principle, the overall reaction mechanism in Zn-iodine batteries involves the stripping/deposition of Zn metal anode and the redox of I^-/I^0 following a solid-liquid conversion path[13-15]. At the cathode side, I^- is firstly oxidized to I_2(s) *via* a two-electron transfer process, forming a layer of solid aggregation at the interface between electrode/electrolyte, subsequently, I^- needs to cross the solid I_2(s) layer obeying a Grotthuss-like hopping mechanism for further oxidation and unavoidably complex with I_2(s) to produce dissolvable polyiodides (I_3^-, I_5^- *etc.*). In this whole reaction process, there are two main issues that hinder the development of Zn-iodine batteries:

Firstly, the generated soluble polyiodides at the cathode side will diffuse across the separator to the Zn anode, causing severe corrosion and promoting side reactions, which leads to low Coulombic efficiency and unsatisfactory cycling performance [16-19]. Such shuttle effect of polyiodides has become the most attracting issue. To address this dilemma, the commonly used strategies are adopting porous carbon as iodine host material *via* physical adsorption[20]. Nevertheless, special attentions on pore size, structure and distribution are required because of the weak attraction between non-polar carbon and iodine species. By comparison, stronger iodine adsorption can be achieved by organic materials or functional substrates through chemical bonding of H-I, N-I and O-I[21-23]. However, the loss of active iodine is inevitable after numerous charging/discharging cycles owing to the irreversible formation of the iodine-containing complex.

Secondly, the accumulation of solid iodine with poor electron conductivity (10^{-6} to 10^{-9} S cm^{-1}) generates a passivation layer on the electrode surface, limiting the charge transfer process and slowing down cathodic reactions[24, 25]. Although recent efforts have been made to develop highly active electrocatalysts for fast iodine conversion, such as single-atom catalysts[26], heteroatom-doping[23] and metal-organic framework[27], the aggregation of solid iodine is unavoidable due to its limited solubility in aqueous electrolytes. Therefore, the state-of-the-art strategies remain great challenge to simultaneously inhibit the polyiodides shuttle and reform the deposition of solid iodine.

Alternatively, biphasic electrolyte (BP) composed of two immiscible solutions, which was primarily applied in redox flow batteries (RFB) to substitute the combination of traditional single-phase electrolytes and ion-exchange membranes, naturally produces an artificial liquid-liquid interface for

[a.] *Jiangsu Key Laboratory of Electrochemical Energy Storage Technologies, College of Materials Science and Technology, Nanjing University of Aeronautics and Astronautics, Nanjing, 210016, China.*
[b.] *Institute of Advanced Materials, Nanjing Tech University, Nanjing 211816, China.*
[c.] *National Key Laboratory of Mechanics and Control for Aerospace Structures, Institute for Frontier Science, Nanjing University of Aeronautics and Astronautics, Nanjing 210016, P.R. China*

Supplementary Information available: [details of any supplementary information available should be included here]. See DOI: 10.1039/x0xx00000x

effectively separating dissolved active species based on their polarities[28-31], offering a clever tactic to address the above-mentioned issues. Recently, the different BP electrolytes of CH_2Cl_2/H_2O[49], acetonitrile (ACN)/$ZnSO_4$[50], ACN-ionic liquids/$ZnSO_4$[51], ionic liquids/H_2O[52] for Zn-iodine batteries were reported to restrict polyiodides. Nevertheless, the effectiveness of these BP electrolytes in portable Zn-iodine batteries is limited and the detailed reaction mechanism involved in organic phase remains unexplored. (i) Owing to reversible and rapid conversation between I_2 and polyiodides, the dissolved polyiodides inevitably contains I_2 components, while it is hard to co-extract I_2 and polyiodides *via* single solvent owing to their different polarity, which results in inefficient confinement of soluble iodine species through BP systems and the fundamental design principles governing the compatibility between solvents and different iodine species remains unknown; (ii) the cathodic reaction of I^-/I^0 proceeds through a solid-liquid conversion path in aqueous electrolyte, while the unexplored reaction mechanism in organic phase deserves detailed study in BP system; (iii) the reported BP Zn-iodine/bromine batteries are still prototypes typically in stationary beaker cells, which is impractical for the design of portable/wearable energy storage devices.

Herein, the co-extraction of iodine and polyiodides is experimentally achieved by polarity coupling in a newly developed BP electrolyte for Zn-iodine batteries. In detail, the BP interface is formed between the immiscible organic ethyl acetate (EA) phase containing bis(trifluoromethanesulfonyl)-imide zinc ($Zn(TFSI)_2$) and aqueous phase of $ZnSO_4$/KI solution, where the dissolved iodine and polyiodides are confined in the organic phase electrolyte (cathode side). The co-extraction of iodine/polyiodides mechanism is explored and correlated to the principle of polarity coupling between iodine species and solvent molecules. Besides, a liquid-liquid conversion route of iodine at the cathodic side in BP electrolyte was revealed by rotating ring electrode (RRE), which is completely distinct from the traditional liquid-solid conversion in aqueous electrolyte, exhibiting much improved charge transfer kinetics. According to these understandings, quasi-solid-state (QSS) portable Zn-iodine batteries featuring a gravity-independent stratified interface based on the BP electrolyte system composed of microspace-confined EA phase and PAM-CMC hydrogel further demonstrate superior cycling stability to other reported BP Zn-I/Br batteries. As proof-of-concept applications, the assembled BP devices are successfully employed to the health monitor under multiple practical operation conditions (**Figure 1**)

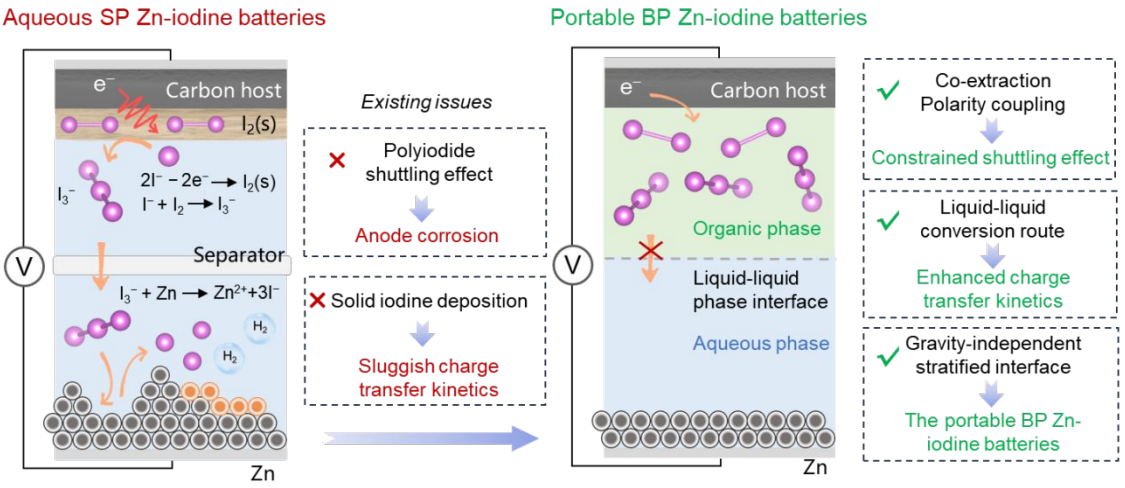

Figure 1. Schematic diagram of the comparison between aqueous SP Zn-iodine batteries and portable BP Zn-iodine batteries

Results and discussion

Iodine (I_2) is a diatomic molecule with symmetric linear shape. Since both I atoms share an equal proportion of charge, the net dipole moment of I_2 comes out to be zero, making it a nonpolar molecule. As a typical polyiodide, triiodide ion (I_3^-) has similar linear configuration with no dipole moment in vapor phase. Nevertheless, the experiment results suggest that I_3^- becomes polarizable and soluble in polar solvent due to the molecule interaction-induced symmetry breaking[32-35]. The differences in polarity make it challenging to co-extract I_2 and polyiodides according to the principle of "like dissolve like". However, in the application of Zn-iodine battery, co-extraction is highly necessary because the cathodic reactions involve the reversible electrochemical conversions between I_2 and polyiodides, since dissolved polyiodides species inevitably contains the I_2 components owing to chemical reaction equilibrium. Unfortunately, the feasibility of constructing BP electrolyte to restrict I_2/polyiodides on the cathode side *via* single solvent and prevent their shuttling remains an unknown question to date. In our experiment, an aqueous solution containing I_2 and I_3^- (0.1 M KI/20 mM I_2) was prepared to simulate dissolved iodine species in aqueous phase and then respectively mixed with a number of solvents with different polarity including petroleum ether (PE), cyclohexane (CH), carbon tetrachloride (CTC), benzene (BZ), ethyl acetate (EA), methyl acetate (MA), pyrrole (Py) and acetonitrile (ACN) (**Figure 2a, 2b**)[36]. After a few seconds, self-stratified phases are produced except for the high polar Py and ACN. Notably, the aqueous phase becomes the lightest yellow upon the addition of EA, indicating the nearly complete extraction of polyiodides/iodine. Direct evidences are provided

by ultraviolet-visible (UV-vis) spectra through quantifying the content of I-species respectively in organic and aqueous phases. Owing to the chemical equilibrium between I_2 and polyiodides, the R value *via* the absorbance changes of I_3^- (288 nm) in aqueous phase (I_3^- *after* and I_3^- *before*) was defined to quantitatively evaluate the extraction ability of different organic solvent for iodine species according to Lambert-Beer law.

$$R = 1 - \frac{A_{(I_3^- \, after)}}{A_{(I_3^- \, before)}}$$

As displayed in **Figure 2c**, the obvious peaks at ~518 nm of PE, CH and CTC phases indicate the presence of I_2, corresponding to the violet color of organic phases. The absorption of I_2 blueshifts to ~504 nm in the case of BZ, giving a color of red-brown due to the stronger molecular interaction with electron transfer from aromatic hydrocarbon to I_2, which is reflected by the newly emerged peak of BZ-I_2 complex at 288 nm[37]. The corresponding intensity changes of I-species in the UV-vis spectra of the aqueous phase after extraction in **Figure 2d** suggest that the non-polar solvents of PE, CH, CTC and BZ exhibit a high selectivity for I_2, while I_3^- cannot be completely extracted into organic phase with R values of 31%, 35%, 50% and 83% respectively (**Figure 2e**). In comparison, both I_3^- (294 and 364 nm) and I_2 (450 nm) are effectively extracted in EA [38, 39], resulting in a calculated R-value of as high as 98%. In the case of MA with similar structure but slightly increased polarity to EA, only I_3^- is detected in MA phase with a comparatively decreased R-value of 88%. In additional, the corresponding absorbances of I_3^- (288 nm) in aqueous phase after extraction by different organic solutions are exhibited in **Figure S1**.

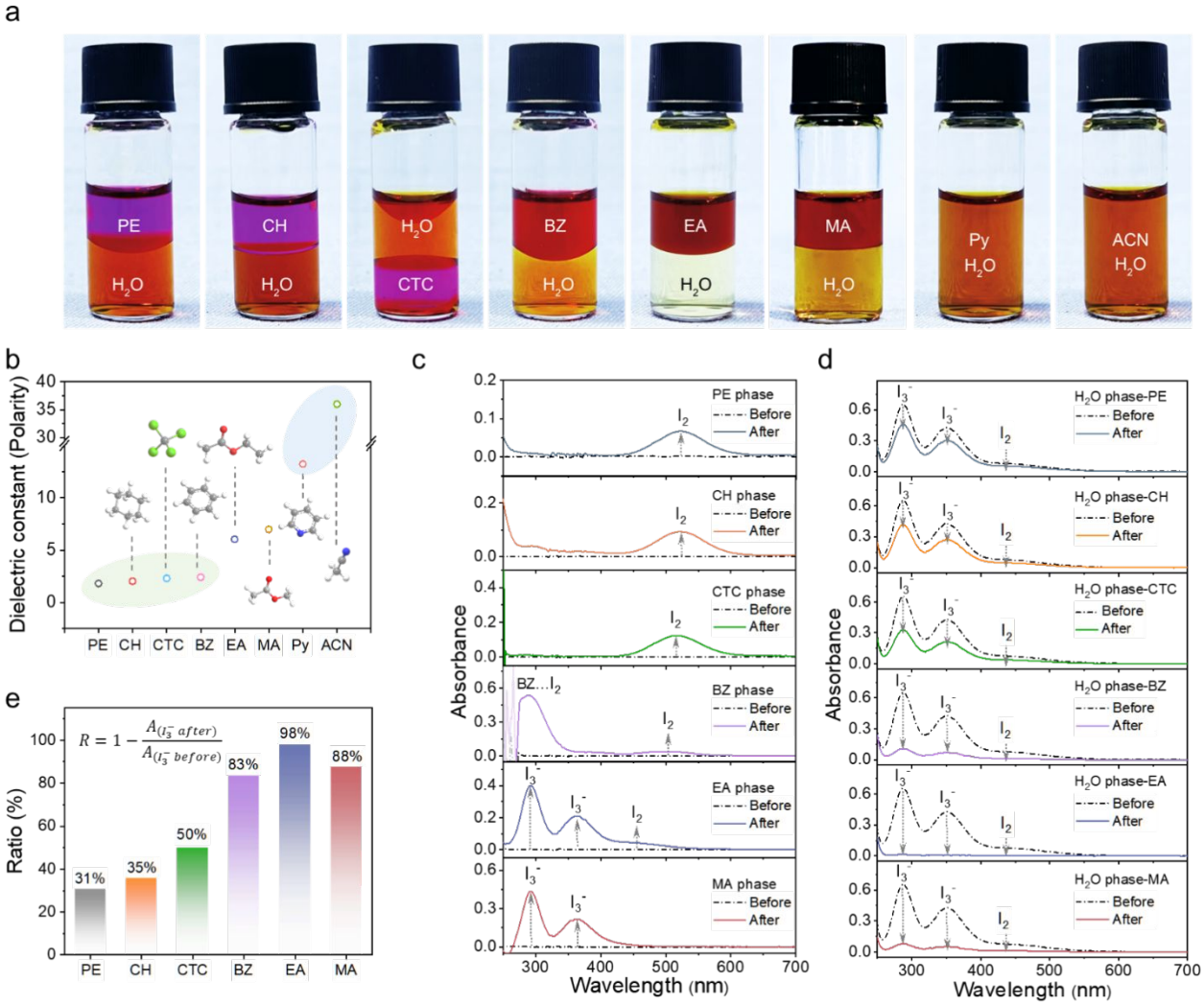

Figure 2 Selection of organic solvents and extraction effects of iodine and polyiodides. (a) The photos of different BP extract systems composed of the organic phase (PE, CH, CTC, BZ, EA, MA, Py and ACN) and 0.1 M KI/20 mM I_2 aqueous phase. (b) The dielectric constants of different organic solvents. The UV-vis spectra of (c) different organic phase and (d) 0.1 M KI/20 mM I_2 aqueous phase before and after extraction. (e) R value of I_3^- peaks of H_2O phase after extraction.

View Article Online
DOI: 10.1039/D5EE02593A

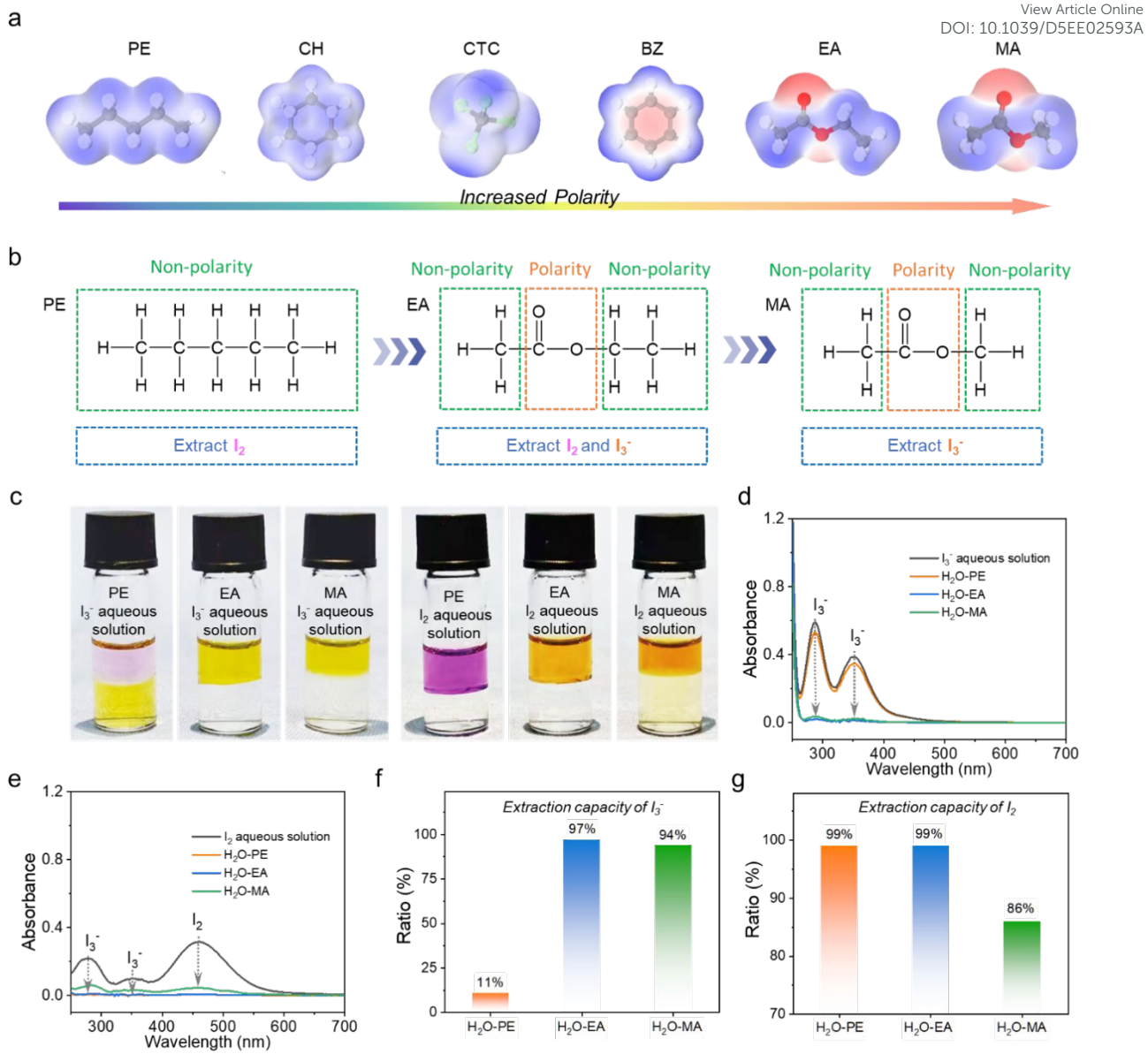

Figure 3. (a) Electrostatic potential distribution of different solvents. (b) The relationship between molecular polarity and iodine species extraction. (c) The photos of different BP extract systems composed of the organic phase (PE, EA, MA) and I_3^- and I_2 aqueous phase. (d-e) The UV-vis spectra of different aqueous phase before and after extraction. (f-g) R values of I_3^- peaks (288 nm) and I_2 peaks (460 nm) of aqueous phase after extraction.

The distinct advantages of EA were validated by analyzing the charge distribution and molecular electrostatic potential (ESP). According to the comparison presented in **Figure 3a** and **Figure S2**. The nonpolar alkyl group and symmetric structure enable the uniform charge distribution in PE, CH, CTC and BZ, while the polar ester group induces the charge separation in EA and MA. Therefore, combined with the experiment results, the principle for the co-extraction of iodine/polyiodides enabled by polarity coupling is summarized in **Figure 3b**. The nonpolar PE with hydrophobic alkyl chains ensures efficient extraction of iodine and facilitates the construction of BP interface, but excludes polyiodides; Py and ACN with strong polarity can homogenously mix with water, unlikely producing phase separation; EA containing both nonpolar hydrophobic alkyl group and polar ester group exhibits moderate molecule polarity and allows the formation of self-stratified BP system with water and simultaneous extraction of iodine and polyiodides. As a control experiment, although MA possesses similar structure to EA, the slightly increased polarity due to the shortened alkyl chain limits the ability to extract iodine, further validating the principle of polarity coupling.

More compelling evidence were obtained through experiment investigating the difference between the non-polarity and polarity groups in extracting I_2 aqueous solution and I_3^- aqueous solution. The I_3^- aqueous solution was prepared by mixing 0.1 M KI and 1 mM I_2; excess KI ensures the nearly complete conversion of I_2 to I_3^-. I_2 aqueous solution was obtained by ultrasonication of solid iodine in water. As shown in **Figure 3c**, PE, EA and MA were mixed with I_3^- aqueous solution and I_2 aqueous solution, respectively, spontaneously producing self-

stratified phases. Taking solution color, R-value and corresponding absorbance changes into consideration (**Figure 3d-3g** and **S3**), it is reasonable to conclude that PE exhibits excellent extraction efficiency for I_2 but weak extraction for I_3^-. Conversely, MA displays good ability for extracting I_3^- together with moderate extraction efficiency for I_2. These results suggest that polar and non-polar functional groups in organic molecules function differently in their tendencies to extract I_2 and I_3^-, Notably, EA demonstrates exceptional capability in extracting I_2 and I_3^- from aqueous solutions because of its well-suited polarity coupling.

Molecular dynamics (MD) simulations were also conducted to investigate the co-extraction ability of EA-H_2O BP system to I_3^- and I_2 (**Figure S4**). I_3^- and I_2 distributed in H_2O phase in the initial state rapidly diffuses to and fully fills in EA phase in the final state, suggesting the strong interaction between I_2/I_3^- and EA. This was further proved by DFT calculation (**Figure S5**). According to molecular orbital theory, an empty antibonding (σ*) orbital is formed in I_2 and I_3^- molecules due to the unique outermost electronic configuration of $5s^25p^5$ in I atom (**Figure S6**)[40, 41], which is prone to accept the donated lone-pair electrons from the negatively charged C=O/C-O. Such a charge transfer behavior between EA and I_3^-/I_2 is clearly evidenced in the optimized charge-density-difference pattern (**Figure S7**).

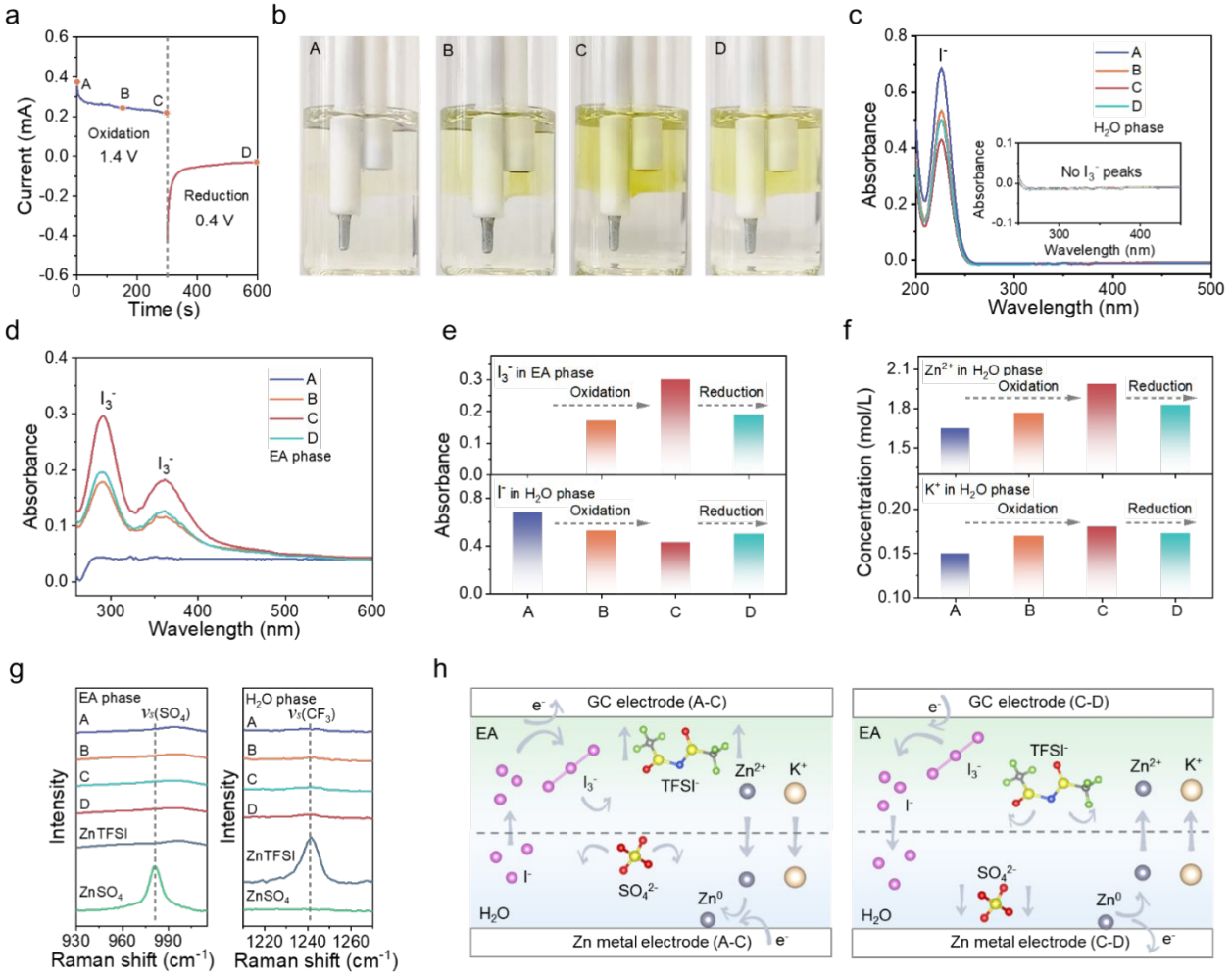

Figure 4. Characterization of ion transport behavior across the interface of BP electrolyte. (a) The CA curves marked with four represented states (A, B, C and D). (b) The digital photos of visualized two electrode system corresponding to the states of A-D. The UV-vis spectra in the states of A-D of (c) EA phase and (d) H_2O phase. The summarized (e) UV-vis absorbance changes of I_3^- in EA phase and I^- in H_2O phase and (f) concentrations changes of Zn^{2+} and K^+ in H_2O phase from states A to D. (g) The Raman spectra of EA phase and H_2O phase in the states of A-D, 1 M $ZnSO_4$ in H_2O and 1 M $Zn(TFSI)_2$ in EA. (h) The schematic of the ion transport mechanism during the charging-discharging process.

In order to ensure an enough high ionic conductivity of EA phase, $Zn(TFSI)_2$ was selected as Zn-salt because the other commonly used ones such as $Zn(ClO_4)_2$, $ZnSO_4$ and $Zn(OTf)_2$ cannot be dissolved in EA due to their relatively strong interaction between anion and cation (**Figure S8**). Consequently, an immiscible BP electrolyte system was successfully prepared by simply mixing 1 M $Zn(TFSI)_2$ in EA and aqueous solution containing 1 M $ZnSO_4$+0.5 M KI (**Figure S9**). The ion conductivity of the obtained upper EA (1 M $Zn(TFSI)_2$) phase is measured to be 14.34 mS cm^{-1} (**Figure S10**), better than most of the reported values for organic electrolytes even though still lower than that of bottom aqueous solution (76.41 mS cm^{-1}).

The redox behavior of iodine in BP electrolyte system is revealed in a visualized two-electrode system with a glass carbon

(GC) as cathode inserted in EA phase (1 M $Zn(TFSI)_2$) and a Zn rod as anode in aqueous phase (1 M $ZnSO_4$+0.5 M KI) (**Figure S11**). Chronoamperometry (CA) was adopted by respectively applying 1.4 V and 0.4 V for 250 s to oxidize and reduce I-species. In the corresponding current-time curve (**Figure 4a**), four representative points of A, B, C and D are selected for the subsequent acquisition to characterize the chemical composition of the resultant products. As shown in **Figure 4b**, yellow polyiodides emerge on the surface of GC electrode and then gradually dissolve in EA phase during the electrochemical oxidation from A to C. Upon switching the polarization voltage to 0.4 V, the color of EA phase continuously fades from C to D state attributable to the reduction of polyiodides. It is noted that the bottom aqueous phase maintains colorless during the whole process, suggesting the effective inhibition of polyiodides shuttling. Comparably, in single phase (SP) aqueous electrolyte (1 M $ZnSO_4$+0.5 M KI), once the polyiodides are generated, they freely diffuse to the anode side without any restriction (**Figure S12**). The UV-vis spectra provide direct evidence for the concentration variation of I^- and I_3^- in organic and aqueous phase (**Figure 4c**, **4d**). In aqueous phase, the content of I^- gradually decreases under oxidation and increases at reduction, without any discernible signal from I_3^- during the entire process. Oppositely, in organic phase, the content of I_3^- gradually increases in the process of oxidation from state A to C and decreases in the process of reduction from state C to D. The UV-vis absorbance of I^- in H_2O phase and I_3^- in EA phase in the different states are summarized in **Figure 4e**. Therefore, it could be concluded that I^- can cross the BP interface and be oxidized at the GC surface, whereas the produced polyiodides are thoroughly restrained in organic phase.

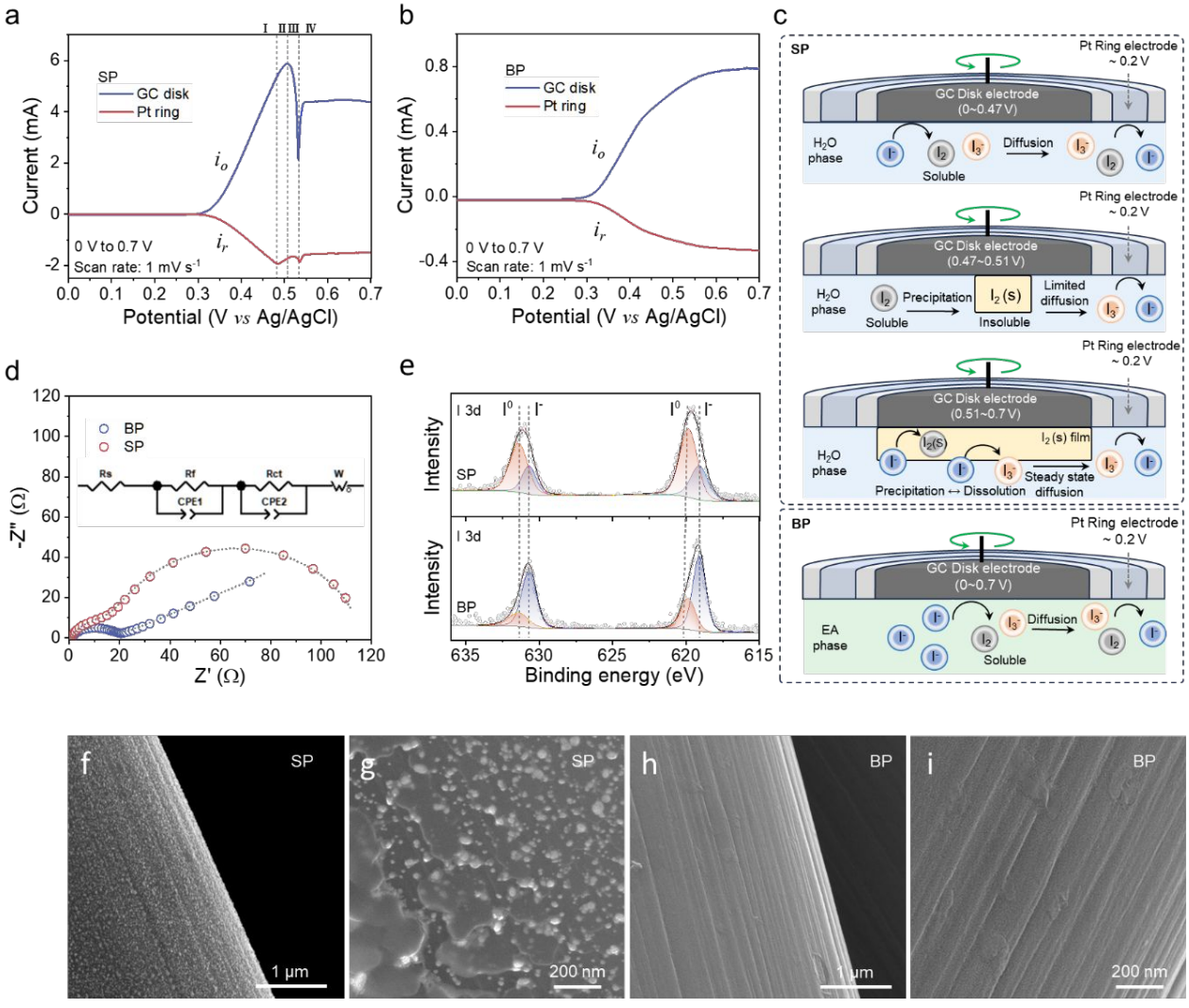

Figure 5 Characterization of cathodic reactions in BP and SP electrolyte. LSVs on RRE in (a) SP and (b) BP electrolyte from 0 V to 0.7 V. (c) The schematic of redox reactions at the interface between the electrode and electrolyte. (d) The EIS plots, (e) XPS spectra and (f-i) SEM images of CC cathode for coin cells based on BP and SP after 15 s polarization under 1.5 V.

Additionally, the inductively coupled plasma mass spectrometry (ICP-MS) and Raman spectra were further utilized to monitor the transport of ions that involves in the charging-discharging process. In **Figure 4f**, the concentrations of K^+ and Zn^{2+} in the aqueous phase increase from states A to C and then decrease from C to D according to the ICP-MS result, indicating the migration of Zn^{2+} and K^+ across the BP interface. Moreover, Raman spectra show typical vibration peaks of S=O at 980 cm^{-1}

View Article Online DOI: 10.1039/D5EE02693A

and C-F at 1240 cm^{-1}, respectively ascribing to SO_4^{2-} and $TFSI^-$ [42-44]. The results displayed in **Figure 4g** indicate that SO_4^{2-} in aqueous phase and $TFSI^-$ in organic phase are not able to cross the BP interface even under electric field. Based on the above analysis, the ion transport mechanism can be concluded in **Figure 4h**. From state A to C, Zn^{2+} and K^+ migrate to the anode side, where Zn^{2+} accepts the electrons and is reduced to Zn^0; I^- moves to the cathode side and is oxidized to generate polyiodides and iodine. Once the polarization voltage is switched to 0.4 V, Zn metal is dissolved in aqueous phase and I_3^- restrained in EA is reduced to I^-, accompanied with the diffusion of Zn^{2+} and K^+ to the cathode side and I^- to the anode side. Besides, $TFSI^-$ and SO_4^{2-} do not cross the BP interface during the charge-discharge process, although they diffuse under the electric field.

In principle, the cathodic reactions of Zn-iodine battery involve the electrochemical conversion of I^-, the complexation between I^- and I_2(s), and the formation of polyiodides in the charging process, which is difficultly detected by traditional spectroscopic techniques. A viable strategy to explore the reaction mechanism occurred at the electrode/electrolyte interface is to use rotating ring disk electrode (RRE: GC disk and Pt ring in this study) as working electrode, coupled with Ag/AgCl as reference electrode and Pt plate as counter electrode (**Figure S13**). Experimentally, SP and BP were respectively utilized as electrolytes, a potential of 0~0.7 V was applied at GC disk, and a constant potential of 0.2 V was held at Pt ring to reduce the iodine species, the rotation speed of the RRE maintains 150 rpm.

Figure 5a shows the linear sweep voltammetry (LSV) curves for the oxidation of I^- in SP electrolyte, which can be divided into four distinct regions: region-I 0~0.48 V, region-II 0.48~0.5 V, region-III 0.5~0.53 V and region-IV 0.53~0.7 V. In region-I, the oxidative current (denoted as i_o) at GC disk corresponding to the conversion from $I^-(aq)$ to $I_3^-(aq)$ through the soluble $I_2(aq)$ and reductive current (denoted as i_r) of $I_3^-(aq)$ to $I^-(aq)$ at Pt ring grow synchronously following the reactions 1 and 2.

$$3I^-(aq) - 2e^- \leftrightarrows I_2(aq) + I^-(aq) \leftrightarrows I_3^-(aq) \quad (1)$$

$$I_3^-(aq) + 2e^- \leftrightarrows 3I^-(aq) \quad (2)$$

The accumulation of $I_2(aq)$ in the vicinity of GC disk leads to the precipitation of solid $I_2(s)$ upon further increase of the potential owing to its limited solubility in aqueous electrolyte as the equilibrium shown in reaction 3.

$$I_2(aq) \leftrightarrows I_2(s) \quad (3)$$

The precipitated $I_2(s)$ on GC disk cannot transport to Pt ring, thus i_r gradually decreases in region-II. Subsequently, further aggregation of $I_2(s)$ on GC disk slows down the oxidation reaction caused by the limited ion diffusion, even though partial dissolution of $I_3^-(aq)$ happens as depicted in reaction 4, thus leading to dramatically decreased i_o and thereafter increased i_r in region-III.

$$I_2(s) + I^-(aq) \leftrightarrows I_3^-(aq) \quad (4)$$

When the formed $I_2(s)$ layer completely covers the surface of GC disk, i_o reaches the lowest point and the manner of $I^-(aq)$ transport changes from direct diffusion to "carrier"-type diffusion in Grotthuss mechanism through $I_2(s)$ film. Finally, both i_o and i_r reach the steady-state in region-IV, indicating the dissolution-precipitation of $I_2(s)$ film attains the equilibrium state. The above analysis supports the solid-liquid reaction route which is in good accordance with our pervious works[45]. Comparably, in the case of BP electrolyte, i_o and i_r monotonously increase and ultimately reach the equilibrium state with the applied potential (**Figure 5b**), indicating a totally different reaction mechanism from that in aqueous SP electrolyte without the presence of $I_2(s)$ owing to the high dissolubility of both I_2 and polyiodides in EA following so-called liquid-liquid conversation route. Such a special mechanism is confirmed by the LSV from 0.7 V to 0 V in **Figure S14**, where a peak attributable to the decomposition of $I_2(s)$ film occurs in SP system rather than in BP system. The above-mentioned reaction mechanisms in SP and BP electrolytes are summarized in **Figure 5c** and **Figure S15** based on the principle that EA with moderate polarity possesses much higher solubility of both I_2 and polyiodides than H_2O, avoiding the aggregation of $I_2(s)$ and realizing the liquid-liquid conversion.

In order to further validate the above mechanism, the coin cells assembled with Zn anode and carbon cloth (CC) cathode separately in BP and SP electrolytes were characterized by CA technique at 1.5 V for 30 s and then their electrochemical impedance spectroscopy (EIS) results are displayed in **Figure 5d**. Obviously, the wide semicircle in the intermediate/low frequency region for the batteries based on SP electrolyte suggests an extra barrier resistance owing to $I_2(s)$ precipitation. Direct evidences can be found in the I 3d XPS spectra (**Figure 5e**) and SEM images (**Figure 5f-5i**) of CC cathode[45, 46], where a stronger I^0 signal is obtained and apparent $I_2(s)$ particles present on the cathode disassembled from the SP-based batteries but not with the BP-based batteries, verifying the cathodic reactions in BP electrolyte follows a different liquid-liquid reaction mechanism.

Although the feasibility of BP electrolyte in prohibiting polyiodides shuttling and the reaction mechanism of I-species in the organic phase have been validated theoretically and experimentally, challenges still remain in the construction of portable Zn-iodine batteries. Firstly, the long diffusion distance of dissolved polyiodides in organic electrolyte leads to irreversible charging/discharging process (**Figure 4b**). Secondly, the gravity-driven stratification is inadequate for complex operational environments. We therefore proposed a QSS portable Zn-iodine battery based on a gravity-independent stratified interface realized by synergistic effect between microspace-confined EA phase in activated carbon (AC) cathode and hydrogel as an aqueous phase to address the above issues (**Figure 6a**). Serving as an effective cathode host, the ultra-high specific surface area (~2198 $cm^2\ g^{-1}$) and organophilic properties of AC enable the rapid absorption of EA electrolyte, and the abundant mesopores (10~20 Å) also could function as reaction micro-vessels, immensely shortening the diffusion distance of dissolved polyiodides and avoiding irreversible redox reactions (**Figure S16**, **S17**). On the other hand, a hydrogel containing 1 M $ZnSO_4$/0.5 M KI is prepared by chemically crosslinking polyacrylamide and carboxymethyl cellulose (PAM-CMC) (**Figure S18**), in which water molecules are constrained in polymeric network, guaranteeing efficient ion diffusion and at the meantime further limiting the diffusion of iodine species. As

displayed in **Figure 6b**, after 24 h, the added I_3^-/I_2 are effectively constrained in EA phase, leaving hydrogel colorless, whereas severe shuttling of I_3^- was observed in water//hydrogel SP system. When PAM-CMC and EA phase were sequentially vialed in a bottom-up manner, forming a distinct interface, it can remain intact upon flipping over and keeps stable even after 30 days (**Figure 6c** and **S19**). Combining with the advantages of AC cathode and PAM-CMC hydrogel, the QSS devices were assembled in the configurations of Zn//hydrogel//AC-EA based on the above BP electrolytes and then electrochemically evaluated at a constant current of 0.5 mA cm^{-2}. *In-situ* Raman spectra confirm the highly reversible reactions at the cathode side with the appearance and disappearance of I_3^- at 110 cm^{-1} and I_5^- at 160 cm^{-1} respectively in the charging and discharging processes (**Figure 6d**). Moreover, almost the same GCD curves at 1 mA cm^{-2} with a high Columbic efficiency of 98.6% are obtained no matter what the batteries work in the way of anode upward or cathode upward, further ensuring the effectiveness of the design in gravity-independent BP-based energy storage system (**Figure S20**).

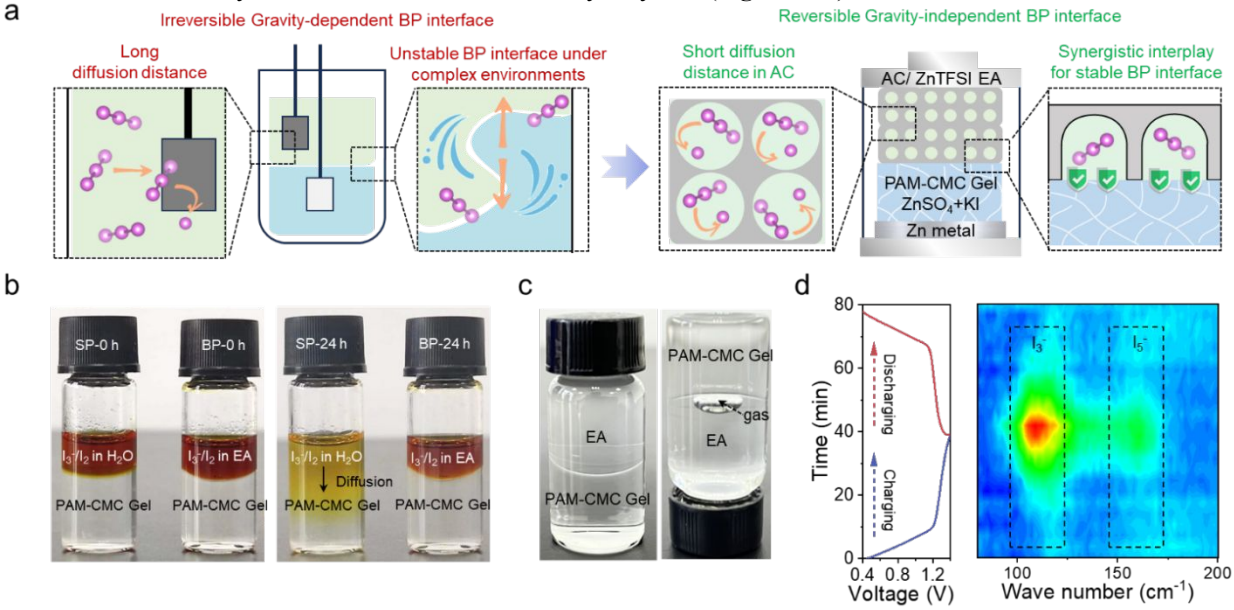

Figure 6 (a) The design of gravity-dependent and gravity-independent BP interface. (b) The photos for shuttle experiment of I_3^-/I_2 in EA/PAM-CMC (BP) and H_2O/PAM-CMC (SP) systems. (c) The photos of gravity-independent test of EA/PAM-CMC. (d) The *in-situ* Raman spectra of Zn-iodine based on BP electrolyte during the charging/discharging process.

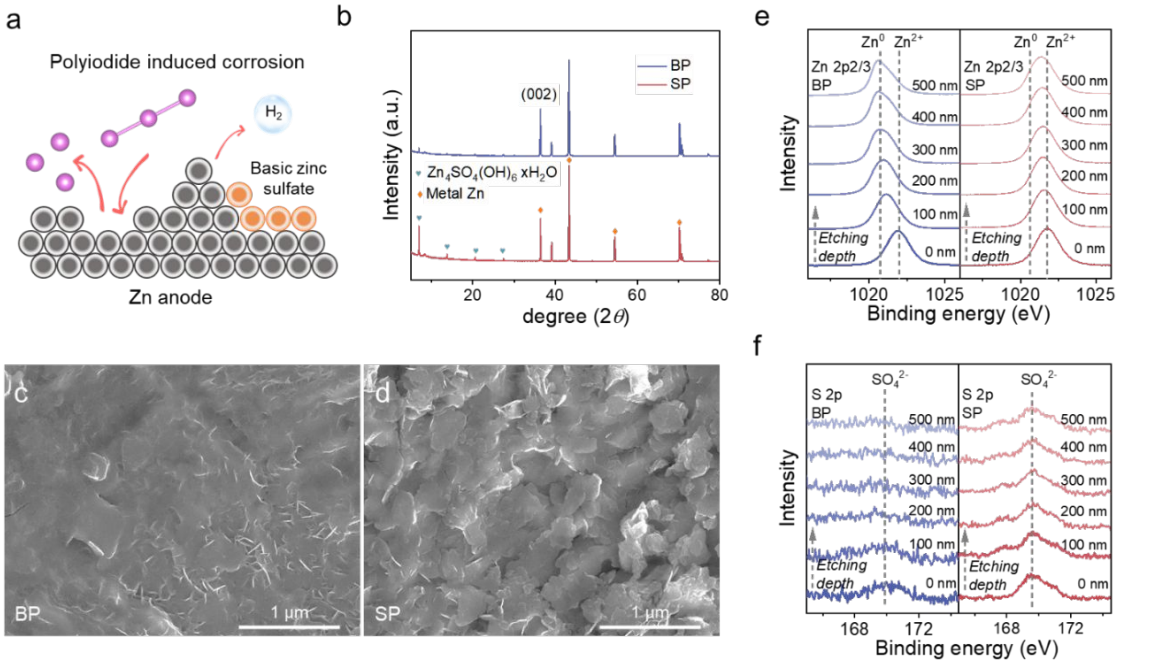

Figure 7 Characterization of anode in BP and SP electrolytes. (a) The schematic diagram of polyiodides induced corrosion at Zn anode surface. (b) The XRD patterns, (c, d) SEM images and the etching XPS results (e) Zn 2p2/3, (f) S 2p of Zn electrodes after 50 cycles in the Zn-iodine batteries based on BP and SP electrolyte.

In our previous study[13], it has been proven that the side reactions occurring on Zn anode mainly originate from the corrosion by dissolvable polyiodides, resulting in highly porous and loose surface which subsequently accelerates hydrogen evolution reaction (HER), consumes protons in aqueous electrolyte, and locally induces the precipitation of $Zn_4SO_4(OH)_6{\cdot}xH_2O$ (**Figure 7a**). Herein, the anodes respectively disassembled from the batteries of Zn//hydrogel//AC (SP) and Zn//hydrogel//AC-EA (BP) after 10 cycles at 0.5 mA cm^{-2} were characterized to verify the suppression to the side reactions by BP electrolyte via restricting the shuttle of polyiodides. The stronger XRD signals ascribed to $Zn_4SO_4(OH)_6{\cdot}xH_2O$ in SP electrolyte reveal the more severe corrosion occurred on Zn anode in comparison with that in BP electrolyte (**Figure 7b** and **Figure S21a**). SEM images also confirm the severe corrosion of Zn anode in SP electrolyte with more platelets generated on the surface (**Figure 7c, 7d** and **Figure S21b**). The composition of the cycled Zn anodes was analyzed in depth direction using X-ray photoelectron spectroscopy (XPS) equipped with an etching technique (**Figure 7e, 7f**). The platelets can be identified as $Zn_4SO_4(OH)_6{\cdot}xH_2O$ with the characteristic peaks of Zn^{2+} at 1023.1 eV and SO_4^{2-} at 169.8 eV at the outermost layer of Zn anodes[22, 47, 48]. It is noteworthy that, according to the emergence of XPS signals of Zn^0 and disappearance of SO_4^{2-}, the corrosion depths of Zn anode disassembled from the BP and SP batteries varies significantly with 100 nm and 500 nm respectively, manifesting the co-extraction of iodine and polyiodides in BP effectively inhibits the side reactions of corrosion and hydrolysis and thereby guarantees a relatively stable electrolyte/anode interface.

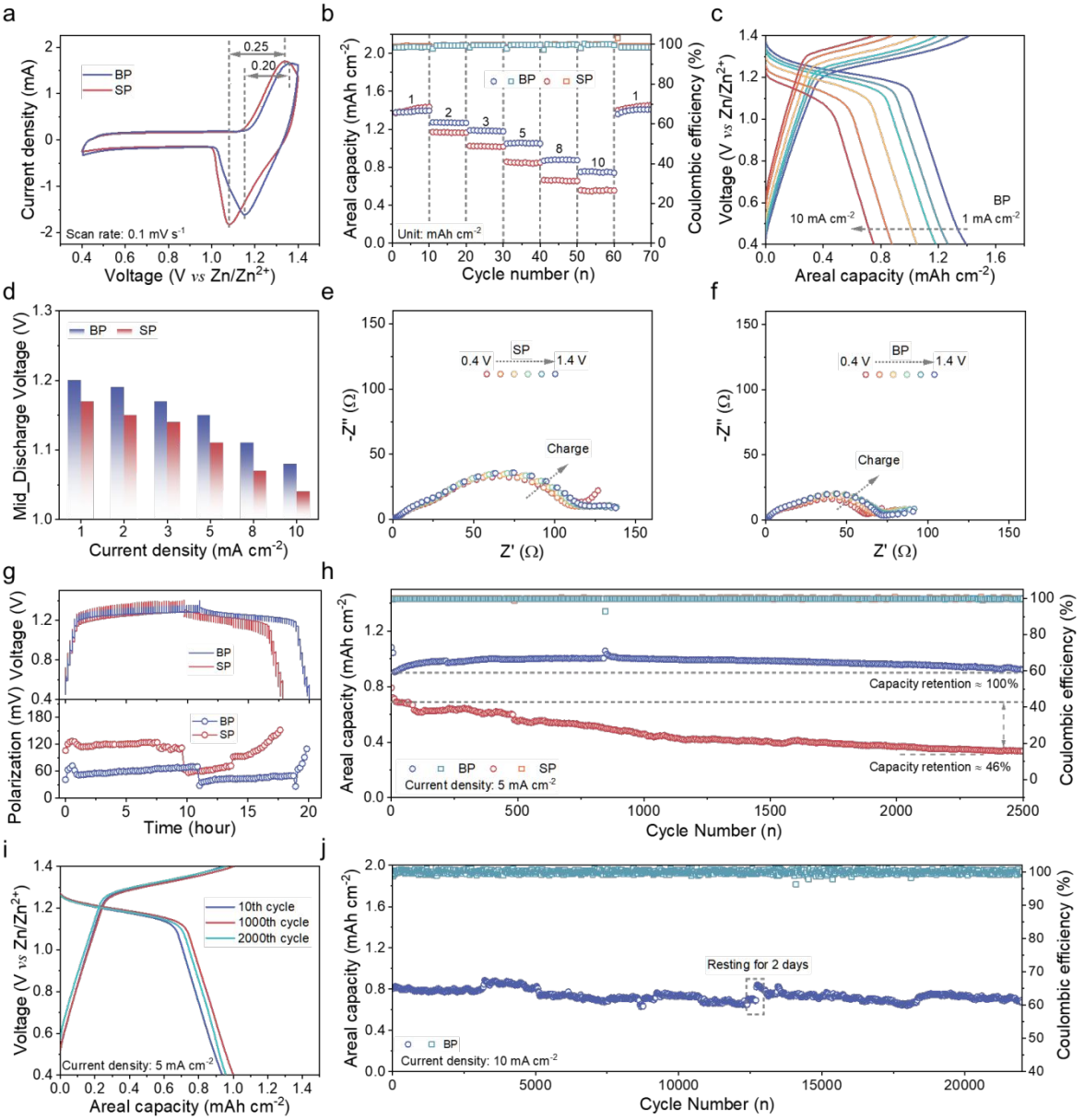

Figure 8 The electrochemical performances of QSS Zn-iodine batteries based on BP and SP electrolyte. (a) The CV curves at 0.1 mV s^{-1}. (b) The rate performance. (c) The GCD curves of BP electrolyte at different current densities. (d) The mid-discharge voltages. (e, f) The *in-situ* EIS spectra during the charging process. (g) The GITT curves. (h) The cycling performance at 5 mA cm^{-2}. (i) The GCD curves of BP electrolyte at 5 mA cm^{-2}. (j) The cycling performance of BP electrolyte at 10 mA cm^{-2}.

View Article Online
DOI: 10.1039/D5EE02595A

The electrochemical performances of QSS Zn-iodine batteries respectively based on BP and SP electrolytes were fully evaluated. The CV curves at 0.1 mV s^{-1} display similar shape and characteristic redox peaks of iodine, yet different voltage gaps between the anodic and cathodic peaks for BP (0.20 V) and SP (0.25 V) electrolytes (**Figure 8a**). Moreover, the anodic peak respectively shifts 80 and 110 mV for BP and SP devices when the scan rate increases from 0.2 mV s^{-1} to 1 mV s^{-1} (**Figure S22**). Both the large voltage gap and anodic peak shift in SP electrolyte are ascribed to the slow electron transfer caused by the formation of solid iodine precipitation. As a consequence, the batteries based on BP electrolyte deliver an areal capacity of 1.40 mAh cm^{-2} at 1 mA cm^{-2} and retain 0.75 mAh cm^{-2} at 10 mA cm^{-2} with a superior retention of 54% compared to 38% of SP device (**Figure 8b**). Besides, the relatively higher mid-discharge voltages at different current densities further demonstrate the fast redox reactions and stable electrode/electrolyte interface in BP system (**Figure 8c, 8d, S23**). The optimized energy/power densities of 1.52 mWh cm^{-2} (at 1.1 mW cm^{-2}) and 9.73 mW cm^{-2} (at 0.73 mWh cm^{-2}) are achieved for Zn-iodine batteries based on BP electrolyte (**Figure S24**).

The *in-situ* EIS tests monitor the resistance changes of QSS Zn-iodine batteries (**Figure 8e, 8f**). Owing to the absence of solid iodine layer, the device based on BP electrolyte demonstrates a much lower charge transfer resistance than that based on SP electrolyte during the charging process, realizing the faster reaction kinetics. As displayed by the galvanostatic intermittent titration technique (GITT), the BP device shows a smaller voltage fluctuation due to the minimized polarization in comparison with the SP device (**Figure 8g**), which agrees well with the results from EIS. Benefiting from the restriction of polyiodides and regulation of cathode surface in BP electrolyte, the assembled cell exhibits significantly enhanced stability with similar GCD curves at 10th, 1000th and 2000th cycles, achieving a 100 % areal capacity retention over 2500 cycles at a current density of 5 mA cm^{-2} (**Figure 8h, 8i**). Even at a high current density of 10 mA cm^{-2}, the batteries perform the outstanding cycling stability over 22000 cycles (**Figure 8j**), which is superior to other reported BP Zn-I/Br batteries (**Table S1**, **S2**), indicating great potential to meet the requirements in practical condition.

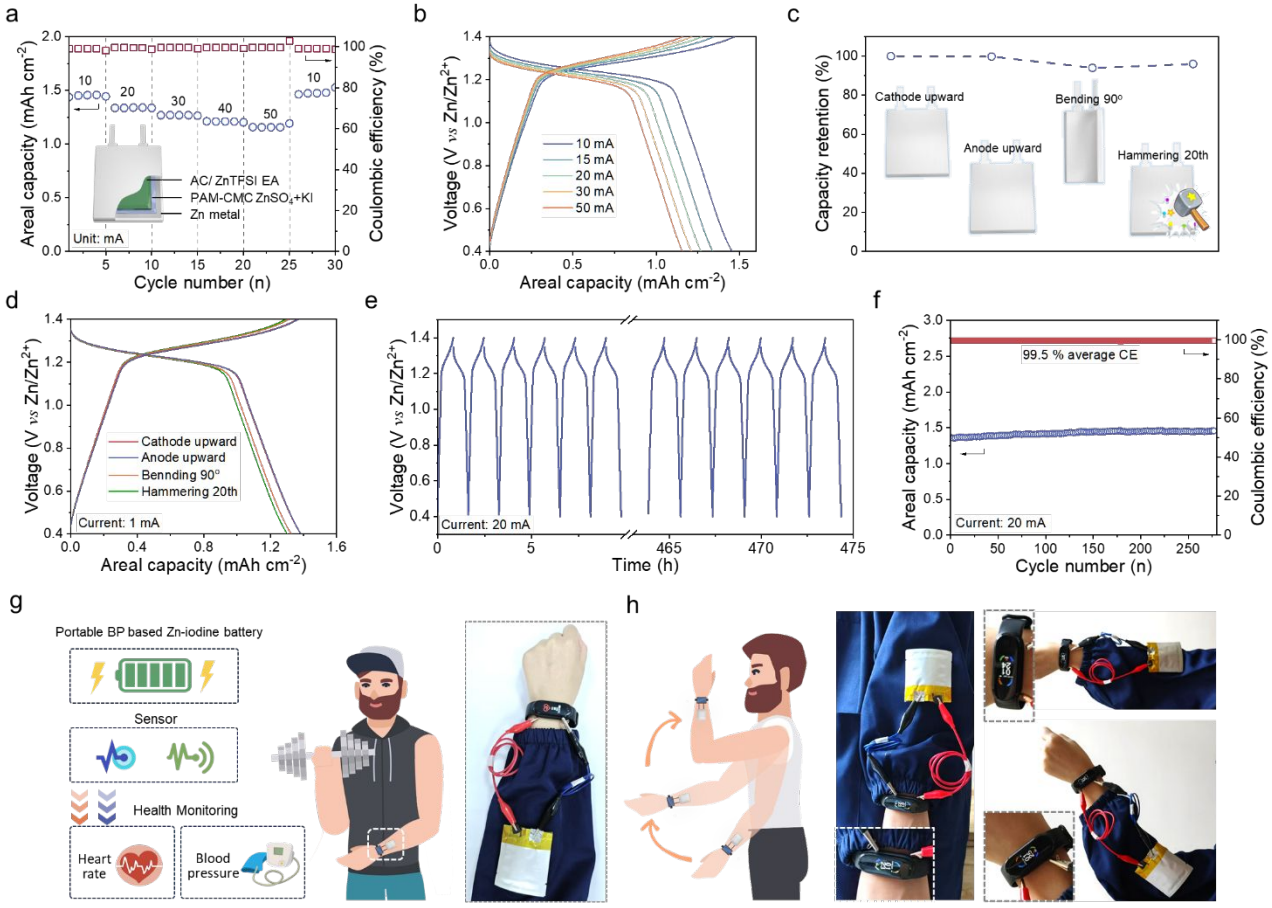

Figure 9 The performance of the QSS pouch cells based on BP electrolyte. (a) The rate performance. (b) the GCD curves from 10 mA to 50 mA. (c) The capacity retentions and (d) GCD curves in different working conditions. (e) The voltage-time curves and (f) cycling performance at 20 mA. (g) Schematic diagram of integrated portable energy storage-sensing system and demonstration photos of health monitoring.

The QSS pouch cells (3 cm×4 cm) of Zn//hydrogel//AC-EA were also fabricated in an aluminum-plastic package. The QSS pouch cells output the areal capacities of 1.45, 1.33, 1.26, 1.20 and 1.15 mAh cm^{-2} with high coulomb efficiency of ~100% at 10, 20, 30, 40, 50 mA, respectively (**Figure 9a, 9b**). The calculated maximum energy density reaches 1.59 mWh cm^{-2}. Benefiting from the special design, the pouch cell exhibits excellent environmental adaptability with 100%, 96% and 98% capacity retentions as the device was inverted, bent (90°), and hammered (for 20 times) (**Figure 9c, 9d**). When the cell was

cycled in a 100% depth of discharge for 450 h (**Figure 9e**), it still can sustain negligible capacity loss with an average coulomb efficiency of 99.5% (**Figure 9f**). Besides, such device maintains stable over 30 cycles of 90° bending-unbending, suggesting its excellent mechanical reliability (**Figure S25**). The portable QSS pouch cells were further integrated with a wearable sensing system for continuous health monitoring. In detail, three QSS pouch cells connected in series offer the capability to safely power a smart watch that can acquire the corresponding data of heart beat and blood pressure (**Figure 9g**). The tandem device mounted on human limb maintains stable operation under various movements. These application measurements demonstrate the feasibility of our rational design for daily usage and potential in a broader context (**Figure 9h**).

Conclusions

In summary, we developed a BP electrolyte system composed of two immiscible solutions of $Zn(TFSI)_2$ in EA and $ZnSO_4$/KI in water to address the key issues of Zn-iodine batteries. Due to the proper nonpolar hydrophobic alkyl chain and polar ester groups, EA with moderate molecule polarity shows the polarity coupling with iodine species, it allows the formation of self-stratified BP system with water and simultaneous extraction of iodine and polyiodides, effectively prevent the shuttling effect of polyiodides. More importantly, multiple spectral characterizations and electrochemical testing disclose that the cathodic reactions follow an unconventional liquid-liquid conversation route without the formation of solid iodine passivating layer, achieving much faster charge transport kinetics. The designed QSS portable Zn-iodine batteries with a gravity-independent stratified interface based on the BP electrolyte with microspace-confined EA and PAM-CMC hydrogel exhibit an enhanced areal capacity of 1.40 mAh cm^{-2} at 1 mA cm^{-2}, excellent rate performance retaining 0.75 mAh cm^{-2} at 10 mA cm^{-2}, 100% capacity retention after 2500 cycles at 5 mA cm^{-2} and cycling stability of over 22,000 cycles at 10 mA cm^{-2}. As proof-of-application, the assembled pouch cell based on BP electrolyte can adapt complex operation environments and realize energy storage supply for human health monitoring.

Author contributions

The manuscript was written through contributions of all authors. All authors have given approval to the final version of the manuscript.

Conflicts of interest

There are no conflicts to declare

Data availability

Data are available upon request from the authors

Acknowledgements

View Article Online
DOI: 10.1039/D5EE02593A

This work was supported by the National Key Research and Development Project Intergovernmental International Science and Technology Innovation Cooperation (2022YFE0109400), National Key Research and Development Program of China (2023YFB2405800) and Leading Edge Technology of Jiangsu Province (BK20232022, BK20220009). This work was supported by the facilities in the Center for Microscopy and Analysis at Nanjing University of Aeronautics and Astronautics.

References

1. S. Ding, T. Saha, L. Yin, R. Liu, M. I. Khan, A.-Y. Chang, H. Lee, H. Zhao, Y. Liu and A. S. Nazemi, *Nat. Electron.* 2024, **7**, 1-12.
2. C. Lu, H. Jiang, X. Cheng, J. He, Y. Long, Y. Chang, X. Gong, K. Zhang, J. Li and Z. Zhu, *Nature* 2024, **629**, 1-6.
3. S. Saifi, X. Xiao, S. Cheng, H. Guo, J. Zhang, P. Müller-Buschbaum, G. Zhou, X. Xu and H.-M. Cheng, *Nat. Commun.* 2024, **15**, 6546.
4. K. Zhang, X. Shi, H. Jiang, K. Zeng, Z. Zhou, P. Zhai, L. Zhang and H. Peng, *Nat. Protoc.* 2024, **19**, 1557-1589.
5. C. P. Grey and D. S. Hall, *Nat.* Commun. 2020, **11**, 1-4.
6. F. Duffner, N. Kronemeyer, J. Tübke, J. Leker, M. Winter and R. Schmuch, *Nat. Energy* 2021, **6**, 123-134.
7. J. T. Frith, M. J. Lacey and U. Ulissi, *Nat. Commun.* 2023, **14**, 420.
8. J. L. Guelfo, P. L. Ferguson, J. Beck, M. Chernick, A. Doria-Manzur, P. W. Faught, T. Flug, E. P. Gray, N. Jayasundara and D. R. U. Knappe, *Nat. Commun.*, 2024, **15**, 5548.
9. D. Han, C. Cui, K. Zhang, Z. Wang, J. Gao, Y. Guo, Z. Zhang, S. Wu, L. Yin, Z. Weng, F. Kang and Q. H. Yang, *Nat. Sustain.* 2021, **5**, 205-213.
10. Q. Cao, Y. Gao, J. Pu, X. Zhao, Y. Wang, J. Chen and C. Guan, *Nat. Commun.* 2023, **14**, 641.
11. R. Zhang, H. Xu, H. Dou and X. Zhang, *Adv. Funct. Mater.* 2024, **15**, 2416497.
12. H. Wang, L. Zhao, H. Zhang, Y. Liu, L. Yang, F. Li, W. Liu, X. Dong, X. Li and Z. Li, *Energy Environ. Sci.* 2022, **15**, 311-319.
13. H. Xu, R. Zhang, D. Luo, J. Wang, H. Dou, X. Zhang and G. Sun, *ACS Nano*, 2023, **17**, 25291-25300.
14. Y. Zhao, Y. Li, J. Mao, Z. Yi, N. Mubarak, Y. Zheng, J.-K. Kim and Q. Chen, *J. Mater. Chem. A* 2022, **10**, 14090-14097.
15. C. Prehal, H. Fitzek, G. Kothleitner, V. Presser, B. Gollas, S. A. Freunberger and Q. Abbas, *Nat. Commun.* 2020, **11**, 4838.
16. H. Wu, J. Hao, S. Zhang, Y. Jiang, Y. Zhu, J. Liu, K. Davey and S. Z. Qiao, *J. Am. Chem. Soc.* 2024, **146**, 16601-16608.
17. J. Hao, S. Zhang, H. Wu, L. Yuan, K. Davey and S. Z. Qiao, *Chem. Soc. Rev.* 2024, **53**, 4312-4332.
18 D. Lin and Y. Li, *Adv. Mater.* 2022, 34, 2108856.
19. R. Zhang, H. Xu, D. Luo, J. Wang, H. Dou and X. Zhang, *Energy Storage Mater.* 2024, **67**, 103294.
20. H. Yu, Z. Wang, R. Zheng, L. Yan, L. Zhang and J. Shu, *Angew. Chem. Int. Ed.* 2023, **62**, e202308397.
21. L. Zhang, M. Zhang, H. Guo, Z. Tian, L. Ge, G. He, J. Huang, J. Wang, T. Liu, I. P. Parkin and F. Lai, *Adv. Sci.* 2022, **9**, 2105598.
22. S. J. Zhang, J. Hao, H. Li, P. F. Zhang, Z. W. Yin, Y. Y. Li, B. Zhang, Z. Lin and S. Z. Qiao, *Adv. Mater.* 2022, **34**, 2201716.
23. J. He, H. Hong, S. Hu, X. Zhao, G. Qu, L. Zeng and H. Li, *Nano Energy* 2024, **119**, 109096.
24. X. Yang, H. Fan, F. Hu, S. Chen, K. Yan and L. Ma, *Nano-Micro Lett.* 2023, **15**, 126.

View Article Online
DOI: 10.1039/D5EE02593A

25. S. Yang, X. Guo, H. Lv, C. Han, A. Chen, Z. Tang, X. Li, C. Zhi and H. Li, *ACS Nano* 2022, **16**, 13554-13572.
26. M. Liu, Q. Chen, X. Cao, D. Tan, J. Ma and J. Zhang, *J. Am. Chem. Soc.* 2022, **144**, 21683-21691.
27. L. Ma, Y. Ying, S. Chen, Z. Huang, X. Li, H. Huang and C. Zhi, *Angew. Chem. Int. Ed.* 2021, **60**, 3791-3798.
28. Vanýsek P, BASÁEZ RAMÍREZ L. *J. Chil. Chem. Soc.* 2008, ***53***, 1455-1463.
29. P. Navalpotro, N. Sierra, C. Trujillo, I. Montes, J. Palma and R. Marcilla, *ACS Appl. Mater. Inter.* 2018, **10**, 41246-41256.
30. J. Meng, Q. Tang, L. Zhou, C. Zhao, M. Chen, Y. Shen, J. Zhou, G. Feng, Y. Shen and Y. Huang, *Joule*, 2020, **4**, 953-966.
31. A. F. Molina Osorio, A. Gamero Quijano, P. Peljo and M. D. Scanlon, *Curr. Opin. Electrochem.* 2020, **21**, 100-108.
32. R. M. Lynden Bell, R. Kosloff, S. Ruhman, D. Danovich and J. Vala, *J. Chem. Phys.* 1998, **109**, 9928-9937.
33. F. S. Zhang and R. M. Lynden Bell, *Eur. Phys. J. D.* 2005, **34**, 129-132.
34. G. Manca, A. Ienco and C. Mealli, *Cryst. Growth Des.* 2012, **12**, 1762-1771.
35. C. J. Margulis, D. F. Coker and R. M. Lynden Bell, *Chem. Phys. Lett.* 2001, **341**, 557-560.
36. J. P. Cerón Carrasco, D. Jacquemin, C. Laurence, A. Planchat, C. Reichardt and K. Sraïdi, *J. Phys. Org. Chem.* 2014, **27**, 512-518.
37. H. A. Benesi and J. H. Hildebrand, *J. Am. Chem. Soc.* 1949, **71**, 2703-2707.
38. M. Telfah, A. A. Ahmad, A. M. Alsaad, Q. M. Al-Bataineh and A. Telfah, *Polym. Bull.* 2022, **79**, 10803-10822.
39. H. Naorem and S. D. Devi, *Spectrochim. Acta A Mol. Biomol. Spectrosc.* 2013, **101**, 67-73.
40. J. Ma, M. Liu, Y. He and J. Zhang, *Angew. Chem. Int. Ed.* 2021, **60**, 12636-12647.
41. D. Li, T. Xia, W. Feng and L. Cheng, *RSC Adv.* 2021, **11**, 32852-32860.
42. H. Wang, X. Liu, J. Zhong, L. Du, S. Yun, X. Zhang, Y. Gao and L. Kang, *Small*, 2024, **20**, 2306947.
43. A. C. Hayes, P. Kruus and W. A. Adams, *J. Solution Chem.* 1984, **13**, 61-75.
44. I. Rey, J. C. Lassègues, J. Grondin and L. Servant, *Electrochim. Acta*, 1998, **43**, 1505-1510.
45. D. Zhao, Q. Zhu, Q. Zhou, W. Zhang, Y. Yu, S. Chen and Z. Ren, *Energy Environ. Mater.* 2024, **7**, e12522.
46. Q. Deng, F. Liu, X. Wu, C. Li, W. Zhou and B. Long, *J. Energy Chem.* 2024, **89**, 670-678.
47. M. Prabakaran, S. Ramesh and V. Periasamy, *J. Adhes. Sci. Technol.* 2016, **30**, 24-44.
48. Z. Hou, M. Dong, Y. Xiong, X. Zhang, H. Ao, M. Liu, Y. Zhu and Y. Qian, *Small*, 2020, **16**, 2001228.
49. J. Zou, G. Wang, S. Lin, H. Yang, X. Ma, H. Ji, S. Zhu, Y. Lyu, C. Wang and Y. Zhou, *Adv. Funct. Mater.* 2024, **34**, 2415607.
50. X. Hu, Z. Zhao, Y. Yang, H. Zhang, G. Lai, B. Lu, P. Zhou, L. Chen and J. Zhou, *InfoMat.* **2024**, 6, e12620.
51. L. Zhang, H. Ding, H. Gao, J. Gong, H. Guo, S. Zhang, Y. Yu, G. He, T. Deng and I. P. Parkin, *Energy Environ. Sci.* 2025, **18**, 2462-2473.
52. K. Zhang, Y. Ge, Q. Yu, P. Zhang, Y. Feng, Z. Tie, J. Ma and Z. Jin, *Energy Storage Mater.* 2024, **67**, 103296.

View Article Online
DOI: 10.1039/D5EE02593A

Data availability

Data are available upon request from the authors.